Chemical Science

ROYAL SOCIETY OF CHEMISTRY

EDGE ARTICLE

View Article Online
View Journal | View Issue

Cite this: *Chem. Sci.*, 2023, **14**, 7170

All publication charges for this article have been paid for by the Royal Society of Chemistry

A near-infrared light-activatable Ru(II)-coumarin photosensitizer active under hypoxic conditions†

Enrique Ortega-Forte,[a] Anna Rovira,[b] Marta López-Corrales,[b] Alba Hernández-García,[a] Francisco José Ballester,[a] Eduardo Izquierdo-García,[bc] Mireia Jordà-Redondo,[d] Manel Bosch,[e] Santi Nonell,[d] María Dolores Santana,[a] José Ruiz,*[a] Vicente Marchán*[b] and Gilles Gasser*[c]

Photodynamic therapy (PDT) represents a promising approach for cancer treatment. However, the oxygen dependency of PDT to generate reactive oxygen species (ROS) hampers its therapeutic efficacy, especially against hypoxic solid tumors. In addition, some photosensitizers (PSs) have dark toxicity and are only activatable with short wavelengths such as blue or UV-light, which suffer from poor tissue penetration. Herein, we developed a novel hypoxia-active PS with operability in the near-infrared (NIR) region based on the conjugation of a cyclometalated Ru(II) polypyridyl complex of the type [Ru(C^N)(N^N)$_2$] to a NIR-emitting COUPY dye. The novel Ru(II)-coumarin conjugate exhibits water-solubility, dark stability in biological media and high photostability along with advantageous luminescent properties that facilitate both bioimaging and phototherapy. Spectroscopic and photobiological studies revealed that this conjugate efficiently generates singlet oxygen and superoxide radical anions, thereby achieving high photoactivity toward cancer cells upon highly-penetrating 740 nm light irradiation even under hypoxic environments (2% O_2). The induction of ROS-mediated cancer cell death upon low-energy wavelength irradiation along with the low dark toxicity exerted by this Ru(II)-coumarin conjugate could circumvent tissue penetration issues while alleviating the hypoxia limitation of PDT. As such, this strategy could pave the way to the development of novel NIR- and hypoxia-active Ru(II)-based theragnostic PSs fuelled by the conjugation of tunable, low molecular-weight COUPY fluorophores.

Received 7th April 2023
Accepted 8th June 2023

DOI: 10.1039/d3sc01844j

rsc.li/chemical-science

1. Introduction

Photodynamic therapy (PDT) represents a promising anticancer therapy.[1] In PDT, a light-responsive photosensitizer (PS) generates reactive oxygen species (ROS), which mediate cell death induction. Depending on the mechanism of action of the PS, PDT can be classified in type I or type II (Fig. 1a). Most current PDT agents predominantly operate *via* a type II mechanism, which relies on surrounding oxygen to form highly cytotoxic singlet oxygen ($^1O_2$).[2,3] However, the oxygen-dependent nature of type II-PDT hampers its therapeutic efficacy due to the hypoxic environment of solid tumors.[4,5] In contrast to the energy transfer process of the type II mechanism, type I-PDT involves light-induced electron transfer from the PS to surrounding biological substrates to produce cytotoxic ROS such as superoxide ($O_2^{\bullet-}$), hydroxyl ($OH^{\bullet}$), or hydroperoxyl $HO_2^{\bullet}$. In this sense, novel and photostable PDT PSs operating simultaneously through efficient type I and type II mechanisms are highly desirable to combat deep-seated hypoxic tumors. To date, only a few reports have described PDT PSs active upon hypoxia.[6–12] We note that photoactivated chemotherapy (PACT) allows treatment of hypoxic tumors.[13–16] However, contrary to PDT, it is not a catalytic process, although it has been demonstrated that some PACT agents may have a double action through the release of an active agent and $^1O_2$ production.[17–20]

The wavelength of the applied light is an important parameter for the clinical delivery of PDT and correlates directly with its penetration capacity into biological tissues. While short-wavelength light in the visible spectrum such as blue (λ = 400–450 nm) or green light (500–550 nm) will penetrate a few

[a]*Departamento de Química Inorgánica, Universidad de Murcia, Biomedical Research Institute of Murcia (IMIB-Arrixaca), E-30071 Murcia, Spain. E-mail: jruiz@um.es*

[b]*Departament de Química Inorgànica i Orgànica, Secció de Química Orgànica, Universitat de Barcelona (UB), Institut de Biomedicina de la Universitat de Barcelona (IBUB), Martí i Franquès 1-11, E-08028 Barcelona, Spain. E-mail: vmarchan@ub.edu*

[c]*Chimie ParisTech, PSL University, CNRS, Institute of Chemistry for Life and Health Sciences, Laboratory for Inorganic Chemical Biology, F-75005 Paris, France. E-mail: gilles.gasser@chimieparistech.psl.eu*

[d]*Institut Químic de Sarrià, Universitat Ramon Llull, Vía Augusta 390, E-08017 Barcelona, Spain*

[e]*Unitat de Microscòpia Òptica Avançada, Centres Científics i Tecnològics, Universitat de Barcelona, Av. Diagonal 643, E-08028 Barcelona, Spain*

† Electronic supplementary information (ESI) available: Additional tables and figures for photophysical and photochemical characterization of the compounds and copies of NMR and MS spectra. See DOI: https://doi.org/10.1039/d3sc01844j

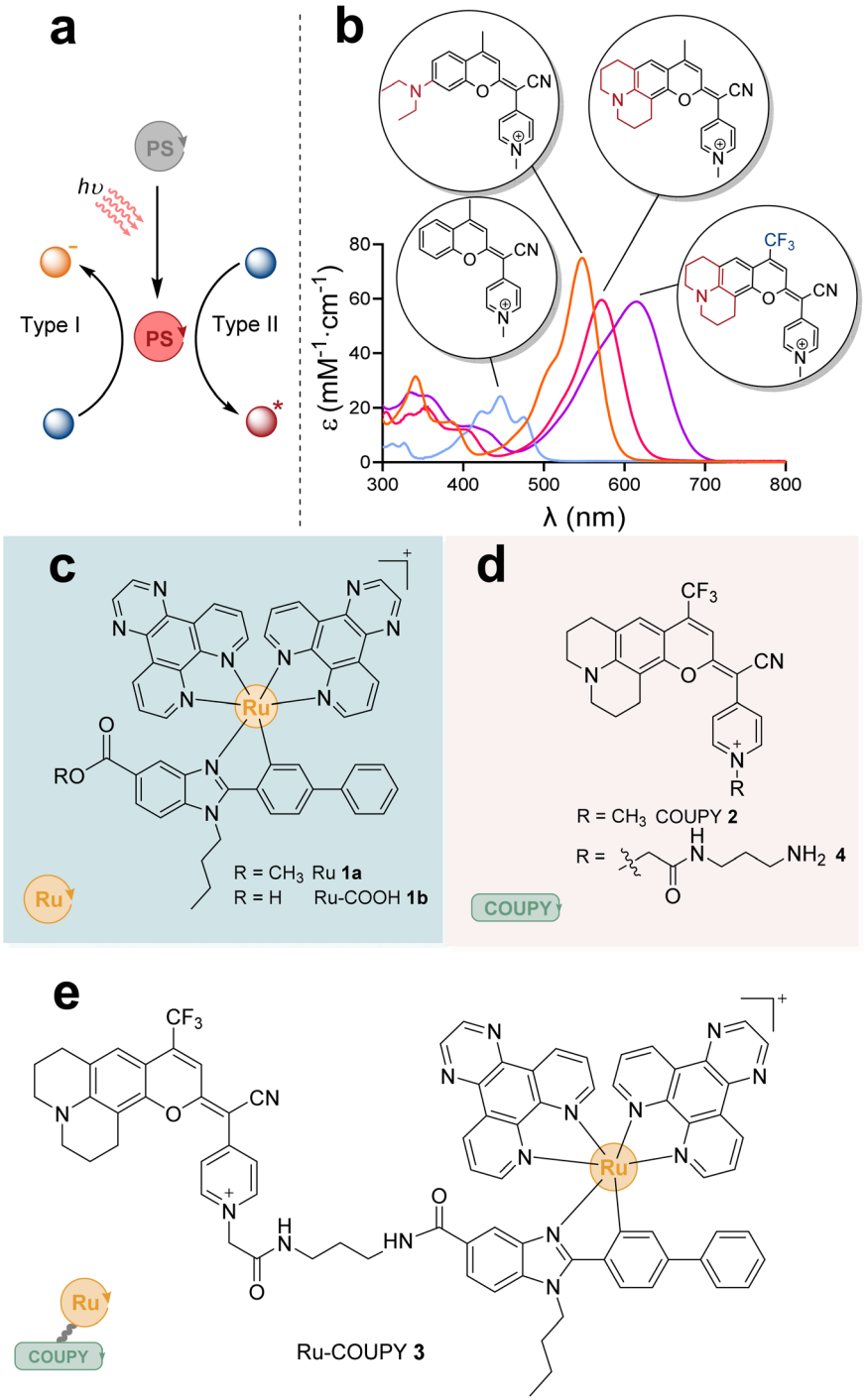

Fig. 1 Rational design of **Ru-COUPY** conjugate for anticancer PDT. (a) Electron-(Type I) and energy-transfer (Type II) mechanisms of PDT. (b) Tunability of the coumarin scaffold and UV-vis absorption spectra of some COUPY fluorophores. (c–e) Structures of the investigated compounds: Ru(II) complexes (**1a** and **1b**), COUPY coumarins (**2** and **4**) and **Ru-COUPY** conjugate (**3**).

hundreds of micrometres into tissues, light of longer wavelengths will penetrate much deeper, typically 3–5 mm for far-red and deep-red light (600–700 nm) and 5–10 mm for near-infrared (NIR) light (700–1000 nm) depending on the tissue.[21–25] Particularly, NIR light minimizes the degree of tissue scattering and reflection and has the advantage of avoiding the absorption band of haemoglobin present in blood vessels.[24] However, even with the use of NIR, light tissue-penetration still represents a major obstacle for oncological PDT, especially for the treatment of large and deep-seated tumors.[25] Despite this limitation, NIR-PDT is still advantageous because it potentially enables the treatment of thicker tumors or deeper cancer lesions compared to photosensitization operating at shorter wavelengths.[26] For instance, the PS lutetium texaphyrin, which entered clinical

trials for prostate cancer, demonstrated high efficacy in treating moderate and large neoplasms *in vivo* (~40 mm^3 and ~147 mm^3 in volume, respectively) following 732 nm light irradiation.[27] The phthalocyanine-based PS, IR-700, conjugated to monoclonal antibodies showed effective growth reduction of large-volume subcutaneous-xenografted tumors after external NIR light irradiation.[28] Hence, NIR-PDT may be suited for the clinical treatment of localized, solid tumors such as head and neck cancers or early-stage localized prostate cancers.[29,30] In fact, the Pd(II)-based PS Padeliporfin (753 nm light-activated) demonstrated efficacy in randomized phase III clinical trials for localized prostate cancer and has been approved by the European Medicines Agency (EMA) for this indication;[31] whereas chlorin-based PS Temoporfin (652 nm light activation) is EMA-approved for head and neck squamous cell carcinoma patients for whom other treatments are insufficient.[25] Lung cancer is another indication for which NIR-PDT is receiving attention.[32,33] Since the lungs are air-containing organs, NIR-PDT *via* endoscopic illumination may be highly effective to treat lung cancer lesions as light is easily transmitted throughout the air.[33,34] In this sense, mono-L-aspartyl chlorin e6 (Talaporfin), a PS activatable with 664 nm light, was approved in Japan in 2004 for early-stage endobronchial cancer.[35] Large, sessile adenomatous polyps as well as colorectal adenomas may also become effective targets for NIR-PDT treatment.[36,37] Other cancer types for which NIR-PDT shows potential clinical utility have been recently reviewed elsewhere.[37–39] In contrast, highly-penetrating NIR light may be unsuited against superficial skin cancers, cutaneous precancerous lesions or some types of bladder cancer since light-promoted photodynamic reactions might occur in the underlying, healthy tissue and cause adverse effects in normal cells.[25,40,41]

Transition metal complexes, especially Ru(II) polypyridyl compounds, have much to offer in the field of oncological PDT due to their intriguing chemical, photophysical and biological properties.[41–47] Compared to conventional PSs used in clinic, mainly based on porphyrin or chlorin scaffolds, metal complexes have been extensively studied owing to their accessibility to various electronic excited-states, which allow efficient ROS-generating PDT reactions.[48–52] However, most of the reported metal-based PSs display dark toxicity and are only activatable with short wavelengths such as blue or UV-light, which are often associated to cell toxicity and poor tissue penetration.[53–56] In this sense, conjugation of suitable organic chromophores to metal complexes have been recently exploited as a promising strategy to extend the absorption and emission of the resulting PS into the phototherapeutic window (600–900 nm).[50] Cyclometalated Ir(III) complexes have been conjugated to boron-dipyrromethene (BODIPY),[57–60] porphyrin,[61] xanthene,[62] and rhodamine fluorophores[63] for this purpose. In addition, some derivatives of the well-established anticancer coumarin scaffold have also been attached to Ir(III) complexes to improve PDT efficacy.[64,65] However, less attention has been paid to the conjugation of organic fluorophores to Ru(II) complexes.[65–69] In this context, we have recently developed a family of coumarin-pyridine (**COUPY**) fluorophores with tunable photophysical properties upon minimal structural modifications (Fig. 1b).[70–72] COUPY fluorophores are also promising fluorescent PDT agents either alone[73] or when conjugated to cyclometalated Ir(III) complexes.[64,72,74]

Based on these antecedents, in this work, we explored the conjugation of a cyclometalated Ru(II) polypyridyl complex of the type [Ru(C^N)(N^N)$_2$] (**1a**, Fig. 1c) to a NIR-emitting COUPY dye (**2**, Fig. 1d) with the aim of developing novel PSs operating in the phototherapeutic window and under hypoxic conditions. We envisioned that the resulting Ru(II)-coumarin conjugate (**3**, Fig. 1e) would induce ROS-mediated cancer cell death upon low-energy wavelength irradiation such as NIR light, which could improve tissue penetration and alleviate the hypoxia limitation of current PDT agents.

2. Results

2.1 Design, synthesis and characterization of the Ru-COUPY conjugate

Based on structure-photophysical property relationships within the COUPY coumarin scaffold[64,73] and on previous results on Ru(II) polypyridyl photosensitizers,[75] we rationally designed the novel PS based on a Ru-coumarin conjugate. On the one hand, as shown in Fig. 1c, we selected a Ru(II) complex containing two dipyrido[3,2-*d*:20,30-*f*]quinoxaline (dpq) N^N ligands and a methyl 1-butyl-2-arylbenzimidazolecarboxylate ligand (**Ru**, **1a**), that was recently described by us as a novel cyclometalated Ru(II) polypyridyl PS with high phototherapeutic potency under hypoxia conditions against HeLa cancer cells following 520 nm light irradiation.[75] On the other hand, with the aim of further red-shifting absorption and emission of the coumarin scaffold to the far-red/NIR region and, consequently, of the resulting Ru(II)-COUPY conjugate, we decided to increase the push–pull character of the fluorophore by modifying the substituents at the positions 4 and 7 of the coumarin skeleton. For this reason, a julolidine-fused CF_3-containing coumarin derivative (**COUPY**, **2**) was selected since both the rigidification of the amino group at the 7-position of the coumarin skeleton together with the incorporation of a strong electron-withdrawing group at position 4 were anticipated to have a strong impact on the photophysical properties of the resulting **COUPY** dye (Fig. 1d).[70,71] As shown in Fig. 1e, the **Ru** conjugate (**Ru-COUPY**, **3**) was assembled *via* the formation of an amide bond between the carboxylic group of Ru(II) complex **1b** and the amino function of a conjugatable version of **COUPY 2** (compound**4**).

First, the required conjugatable COUPY dye **4** was synthesized in four steps starting by reaction of commercially available coumarin **5** with Lawesson's reagent to provide thiocoumarin **6**, which was condensed with 4-pyridylacetonitrile to give compound **7** (Scheme 1). Coumarin **8** was obtained with excellent yield by *N*-alkylation of the pyridine heterocycle with bromoacetamide derivative **9**, which had been previously synthesized by reaction of bromoacetyl bromide with *N*-Boc-1,3-diaminopropane. Then, removal of the Boc protecting group in compound **8** under acidic conditions provided coumarin **4.** On the other hand, the ester group of Ru(II) complex **1a** (ref. 75) was hydrolyzed under basic conditions at 40 °C for 72 h to provide **1b**. Finally, the HATU-mediated conjugation between the

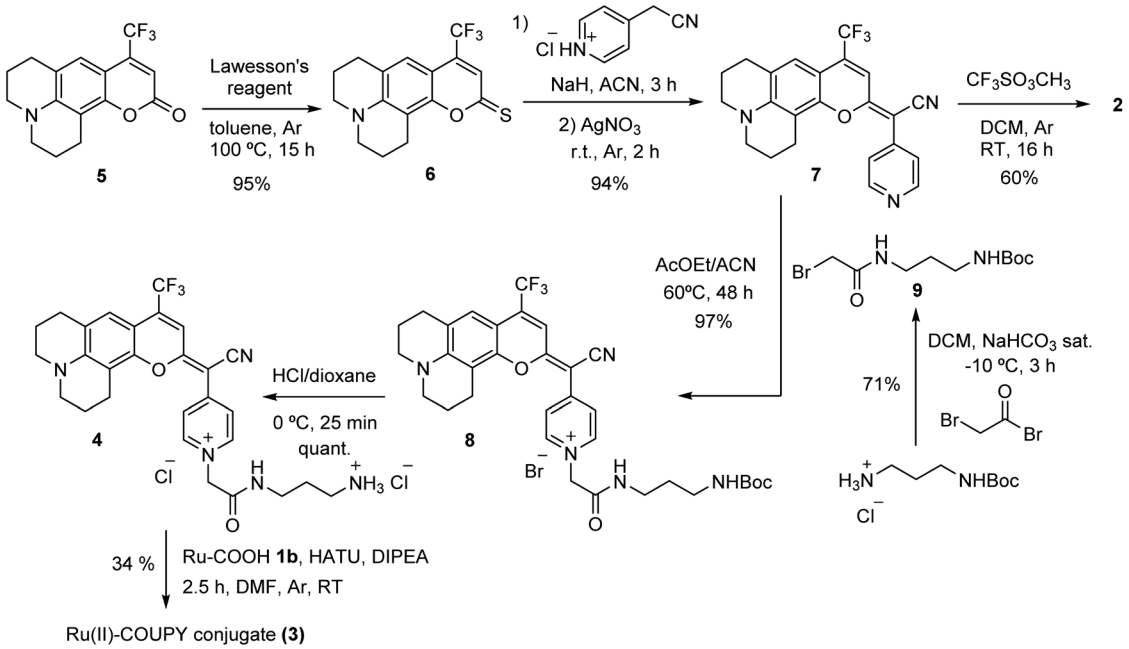

Scheme 1 Synthesis of Ru(II)-COUPY conjugate **3** and of the required COUPY derivatives.

amino-derivatized coumarin **4** and the Ru(II) complex **1b** afforded Ru(II)-COUPY conjugate **3** as a dark blue solid after column chromatography with a 34% yield. For the synthesis of the corresponding *N*-methylated **COUPY** dye **2** to be used as a control compound, coumarin **7** was reacted with methyl trifluoromethanesulfonate in DCM at room temperature yielding the expected compound as a dark blue solid. All of the compounds were fully characterized by high-resolution mass spectrometry (HRMS) and ^{1}H and ^{13}C NMR spectroscopy, and the purity assessed by reversed-phase HPLC-MS analysis (Fig. S1 and S11–S22†).

2.2 Photophysical and photochemical characterization

The photophysical properties (absorption and emission spectra, and fluorescence quantum yield (Φ_F)) of the Ru(II) complex **1a**, the COUPYcoumarin **2** and new Ru(II)-COUPY conjugate **3** (hereinafter **Ru**, **COUPY** and **Ru-COUPY**, respectively) were investigated in acetonitrile (ACN). The UV-vis absorption and emission spectra are shown in Fig. 2 and their photophysical properties are summarized in Table 1. To our delight, the julolidine-fused coumarin analogue containing a trifluoromethyl group at the 4-position (**COUPY**) exhibited absorption and emission maxima in the far-red/NIR region of the electromagnetic spectrum (615 and 691 nm, respectively) (Fig. 1b). An additional red-shift in the absorption (8 nm) and emission (7 nm) maxima occurred after conjugation to the Ru(II) complex, enabling both imaging and PDT evaluation with highly penetrant far-red and NIR light. The fact that the fluorescent quantum yield of **Ru-COUPY** conjugate was smaller than that of the parent **COUPY** suggested the presence of competitive excited-state processes, thereby reproducing the behavior previously found in Ir(III)-COUPY conjugates.[64]

The ability of the compounds to produce singlet oxygen was next evaluated by the observation of the $^{1}O_2$ phosphorescence emission at 1275 nm upon excitation at 355 nm or 532 nm (Table 1). **Ru** was able to generate singlet oxygen in acetonitrile (ACN) and dichloromethane (DCM) but not in aqueous media (PBS buffer). By contrast, neither **COUPY** nor the **Ru-COUPY** produced significant $^{1}O_2$ in any evaluated solvent, either after irradiation with UV or green light, which indicates that conjugation of the **COUPY** fluorophore to the cyclometalated Ru(II) polypyridyl complex had a negative impact on the generation of type II ROS production. Having confirmed that **Ru-COUPY** conjugate did not generate singlet oxygen, we investigated its ability to produce $O_2^{\bullet-}$ by using a spectroscopic method based on the oxidation of the non-fluorescent dihydrorhodamine 123 (DHR123) probe by superoxide anion radical to the fluorescent rhodamine 123 derivative. Although both the **COUPY** and **Ru** alone produce similar amounts of $O_2^{\bullet-}$ after green light irradiation (505 nm) in PBS, conjugation between the fluorophore and the metal complex clearly led to a ~50% increase in the generation of this class of type I ROS (Fig. S2†).

Since previous studies from our laboratories on photosensitizers based on Ir(III)-COUPY conjugates had revealed an efficient excited-state electron-transfer interaction between the redox-active metal complex and the COUPY coumarin,[64,72] we performed transient absorption experiments using laser flash photolysis to get additional insights into the capacity of **Ru-COUPY** to produce $O_2^{\bullet-}$. As shown in Fig. S3,† photoexcitation of the conjugate leads to the formation of a long-lived species in argon-saturated solutions, exceeding the observation time-window of our system, which is not observed in **Ru** nor in **COUPY** (note that ~40% of the transient absorbance signal does not return to the baseline level after 5 milliseconds, unlike for **COUPY**). We hypothesize that the species is a charge-transfer

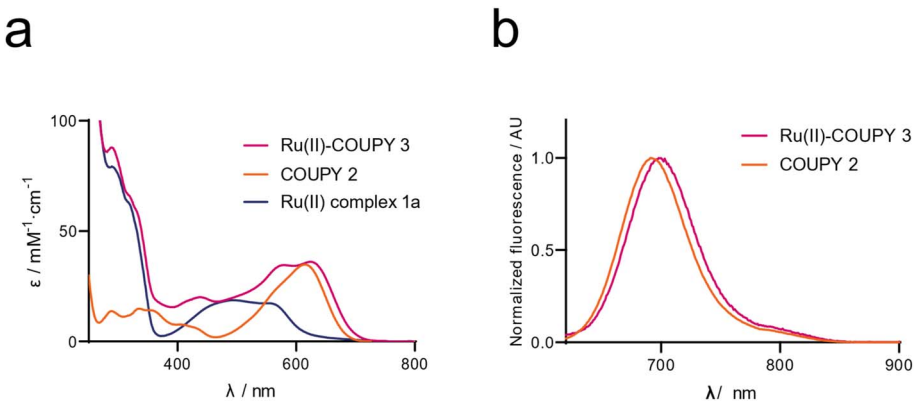

Fig. 2 Comparison of the molar absorptivity of the Ru(II)-COUPYconjugate **3** with that of the unconjugated parent compounds (**1a** and **2**) in ACN (a) and emission spectra of **2** and **3** after excitation at 600 nm in ACN (b).

Table 1 Photophysical and photochemical characterization of compounds **Ru** (**1a**), **COUPY** (**2**) and **Ru-COUPY** (**3**)[a]

	Spectroscopic properties in ACN				Singlet oxygen quantum yield (Φ_Δ)					
	λ_{abs}/nm (ε/mM^{-1} cm^{-1})	λ_{em}/nm	Stokes' shift/ nm	Φ_F	355 nm PBS	532 nm PBS	355 nm ACN	532 nm ACN	355 nm DCM	532 nm DCM
Ru	258(13), 288(14), 321(12), 493(4), 561(17)	n. d.	n. d.	n. d.	≈0	<0.01	0.07	0.09	0.07	0.08
COUPY	615(35)	691	76	0.046	≈0	<0.01	0.01	0.01	0.02	0.01
Ru-COUPY	623(36)	698	75	0.007	≈0	<0.01	≈0	<0.01	0.02	0.02

[a] λ_{abs} absorption maximum, λ_{em} emission maximum, Φ_F fluorescence quantum yield, PBS phosphate buffer saline, ACN acetonitrile, DCM dichloromethane, n. d. not detectable.

state produced by photoinduced electron transfer between the **COUPY** coumarin **2** and the Ru(II) complex **1a** in the conjugate **Ru-COUPY 3**. This novel process would compete with the production of singlet oxygen and should be favoured in polar solvents, which is consistent with the observation that singlet oxygen quantum yields decrease in PBS relative to less-polar solvents (Table 1). The reduced end of the conjugate is expected to react with oxygen to produce superoxide in a secondary electron-transfer step, which should be favoured by its long lifetime. Again, this is consistent with the observation of an enhanced production of superoxide by the conjugate upon irradiation.

The stability of the conjugate was then studied in biological relevant conditions under the dark, *i.e.*, dissolved in complete cell culture medium, finding that **Ru-COUPY** was completely stable after 2 h incubation at 37 °C (Fig. S4†). Next, the photostability of **Ru-COUPY** was evaluated under red light irradiation (620 nm) and compared with that of the parent compounds, namely **Ru** and **COUPY**, as well as of a PS on clinical use (Protoporphyrin IX, **PpIX**). As presented in Fig. S5,† **Ru-COUPY** conjugate exhibits a similar resistance to photobleaching than **PpIX**, being slightly more photostable than the unconjugated Ru(II) complex, which indicates that conjugation of the highly photostable coumarin **COUPY** fluorophore is greatly beneficial both to shift the operability of the PS to the phototherapeutic window and also to increase photostability.

2.3 Cellular uptake and localization

The intracellular uptake of the **Ru-COUPY** conjugate was studied by both inductively-coupled plasma mass spectrometry (ICP-MS) and confocal microscopy (Fig. 3a and b). However, since lipophilicity is known to determine the extent of the cellular uptake and subcellular localization of a given bioactive molecule,[76] we first investigated the lipophilicity of **Ru**, **COUPY** and **Ru-COUPY** by measuring their distribution coefficients between *n*-octanol and water (Table S1†). While the three compounds were mainly found in the organic phase, **Ru** was the most lipophilic one ($\log P = +2.43 \pm 0.27$). Not surprisingly, **COUPY** was the least lipophilic compound ($\log P = +0.36 \pm 0.03$) and, therefore, linking the two moieties through a diamide linker resulted in **Ru-COUPY** having a lower octanol/water distribution coefficient ($\log P = +0.68 \pm 0.08$) than the non-conjugated **Ru** complex.

By taking advantage of the photophysical properties of the coumarin dye, the cellular uptake of **Ru-COUPY** could be tracked in living HeLa cells by confocal microscopy *via* excitation with a red-light laser ($\lambda_{ex} = 633$ nm), being the emission easily detected from 650 to 750 nm. After 30 minutes incubation, luminescence from **Ru-COUPY** was clearly observed in the cytoplasm, mainly in the form of rounded and punctate vesicles (Fig. 3a), which confirmed that the compound was efficiently and rapidly internalized inside cancer cells. **Ru-COUPY** also accumulated in the cell membrane. In contrast, the non-

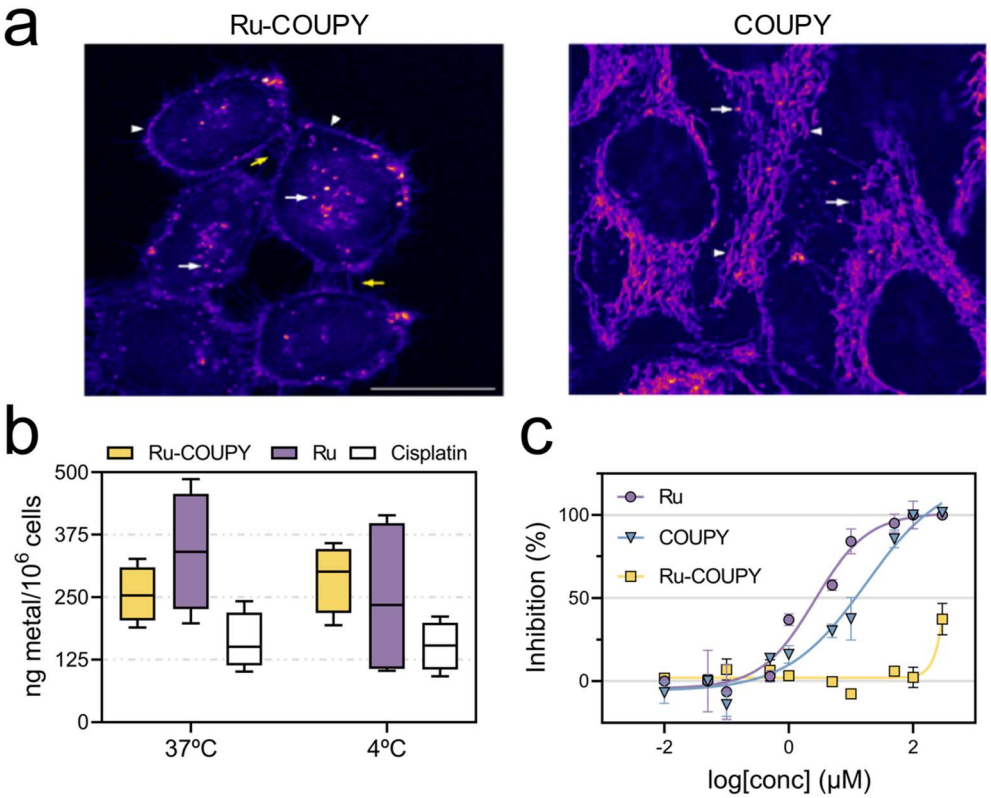

Fig. 3 Cellular uptake and dark cytotoxicity of the **Ru-COUPY** conjugate. (a) Single confocal planes of HeLa cells incubated with the **Ru-COUPY** at 10 μM and **COUPY** at 1 μM for 30 min at 37 °C after excitation at 633 nm. White arrows point out vesicles, white arrowheads cell membrane (left) or mitochondria (right), and yellow arrowheads (left) point out stained filopodial protrusions. Scale bar: 20 μm. (b) Intracellular accumulation of Ru(II) compounds and cisplatin in HT-29 cells after 1 h treatment at 10 μM. Data expressed as mean ± SD from three independent measurements. No statistically significant differences ($p > 0.05$) from two-way ANOVA tests were found in our sample size calculation between treatments and between each condition (37 °C and 4 °C). (c) Dark cytotoxicity curves of **Ru**, **COUPY** and **Ru-COUPY** in HT-29 cells after 24 h expressed as mean ± SD inhibition of cell growth *vs.* dose from three independent replicates.

conjugated **COUPY** dye showed a different location pattern, accumulating preferably in mitochondria, whereas **Ru** could not be observed even when high concentrations were used due the poor emission under red light irradiation. Next, the intracellular amount of **Ru-COUPY** was quantified by ICP-MS and compared with that of the **Ru** precursor. Metal contents found upon incubation with either **Ru-COUPY** or with **Ru** in HT-29 cancer cells were relatively higher to the metal content in cisplatin-treated cells (Fig. S6†). Given that the amount of intracellular ruthenium oscillated in the same range, statistical analysis yielded no significant differences in metal concentration between **Ru-COUPY** and **Ru**-treated cells. Moreover, the uptake of **Ru-COUPY** was not statistically different from **Ru** either at 37 °C nor at 4 °C, where energy-dependent transport is not operative. The similarity in intracellular ruthenium levels regardless of the temperature indicated that active transport was not required for these compounds to enter into cancer cells. In addition, we further investigated the intracellular distribution of **Ru** and **Ru-COUPY** by determining the amount of ruthenium content present in extracted membrane, cytosolic, nuclear and cytoskeleton fractions *via* ICP-MS. As depicted in Fig. S6,† both **Ru** and **Ru-COUPY** were mainly found in the cytoskeleton fractions and, in a lesser extent, in membrane fractions. Minor amounts of metal content were detected in cytosolic and nuclear fractions. This revealed that **Ru** exhibited a similar subcellular distribution as **Ru-COUPY** following cell uptake. However, the percentage of ruthenium trapped in the membrane of **Ru**-treated cells was approximately twice the percentage of those treated with **Ru-COUPY** (37 ± 6% compared to 18 ± 2% over total uptake, respectively).

2.4 Photobiological studies

The photocytotoxicity of **Ru-COUPY** conjugate and its precursors **Ru** and **COUPY** was then screened in a panel of solid-forming tumor cancer cell lines. This screening included two colon cancer cell lines (human HT-29 and murine CT-26) as well as cervix adenocarcinoma cells (HeLa) and ovarian cancer cells (A2780). Dose–response curves from dark and light cytotoxicity were used to calculate the IC_{50} values, which correspond to the concentration needed for inhibition of cell growth by 50%. Phototherapeutic index (PI), calculated as the ratio of dark to light IC_{50} value, was used to measure the actual light-induced anticancer activity.

2.4.1. Dark cytotoxicity. Dark cytotoxicity was first evaluated in the panel of cancer cell lines after a 24 h incubation period. Data from these results are depicted in Fig. S7 and Table

S3.† Fig. 3c illustrates the effect of dark cytotoxicity of the studied compounds on HT-29 cells after 24 h. In general, **Ru** compound showed cytotoxic activities that were markedly higher than that of **COUPY** (IC_{50} values between 0.7–2 μM compared to 17–42 μM, respectively). In contrast, **Ru-COUPY** was deemed as inactive (IC_{50} > 300 μM) after 24 h incubation in HT-29, CT-26 and HeLa cancer cells. The A2780 cells were more sensitive to **Ru-COUPY** treatment, providing an IC_{50} value of 101 μM.

2.4.2. Photocytotoxicity in normoxia at λ_{max}. Photocytotoxicity was next studied in the panel of solid-forming tumor cell lines. Light treatments were applied at 60 mW cm^{-2} using red-light LED source irradiation at 620 nm, which is the maximum wavelength absorption for **Ru-COUPY** conjugate (Fig. 1 and Table 1). Dark cytotoxicity was assayed in parallel upon 1 h incubation with the compounds to test the impact of light treatments (Table S2†); the corresponding dose–response curves being provided in Fig. S7.† In general, all the compounds triggered potent cytotoxicity after 620 nm light exposure in all cancer cell lines (Fig. 4a and Table S2†). Photoactivation of **COUPY** provided submicromolar light IC_{50} values that oscillated between 0.09 and 1 μM, whereas dark IC_{50} values ranged from 35 to 61 μM. Therefore, **COUPY** photocytotoxicity yielded PIs from 35 up to 411 (Table S2†). Light IC_{50} values were even lower for **Ru** complex, ranging from 0.09 to 0.18 μM. Yet PI values for **Ru** were slightly lower in all cancer cells, varying from 9 to 63, given that its cytotoxicity under the dark was more pronounced in all the cell lines, with dark IC_{50} values in the low micromolar range, *i.e.*, 0.8–7 μM (Table S2†). In contrast, the photocytotoxicity of **Ru-COUPY** conjugate was slightly lower than that of the precursors in all cancer cell lines (light IC_{50} values between 0.81–3.1 μM). However, since **Ru-COUPY** did not show dark cytotoxicity, the PI values were comparably higher, ranging from 120 to >300 (Fig. 4a and Table S2†).

Next, a series of *in vitro* cell-based experiments were performed to verify that the source of photocytotoxicity was due to PDT reactions. First, ROS levels were monitored in HT-29 cells by flow cytometry after light irradiation. As expected, treatment with the investigated PSs resulted in overproduction of ROS compared to light-exposed control cells (Fig. S8†). Indeed, this ROS photogeneration level was relatively higher in **Ru-COUPY** conjugate-treated cells than with **Ru** or **COUPY** treatments at equitoxic concentrations. We hypothesize that higher light-induced ROS generation would lead to cell death induction. To further explore this, cellular morphological alterations were studied by quantification of relative cell size and complexity by flow cytometry. Forward (cell size) *versus* side scatter (cell complexity) plot analysis (FSC *vs.* SSC) revealed a population of small cell particles with low FSC/SSC proportion corresponding to dead cells, which is consistent with oxidative damage (Fig. S9†), although other mechanisms might be operating. Finally, since apoptosis is one the main types of cell death associated to photosensitization,[77] cells were labeled with fluorogenic Annexin V after irradiation treatments in the presence of the compounds. All compounds promoted Annexin V^+ populations after light exposure, thereby revealing apoptosis induction (Fig. S10†). Interestingly, the ∼50% increase from **Ru** or **COUPY** PDT treatments to **Ru-COUPY** treatment correlated with the ∼50% increases in superoxide production found with the conjugate (Fig. S2†).

2.4.3. Chromatic phototoxic screening. In view of the promising anticancer photoactive properties of **Ru-COUPY** upon 620 nm light, we decided to investigate photoactivation at longer wavelengths by taking advantage of the extended absorption of the compound in the far-red/NIR region. A chromatic screening was performed using different wavelength irradiation tests following the same protocol. Using a well-by-well LED illumination device, we applied red (620 nm), deep-red (645 nm), far-red (670 nm) and near-infrared (740 nm and 770 nm) light conditions against HT-29 cells. Light treatments in the absence of compounds did not affect cell viability. Data from these results are depicted in Fig. 4b and c and tabulated in Table S4.† The phototherapeutic clinical drug **PpIX** was included as a reference for comparative purposes. All treatments with either **COUPY**, **Ru** or **Ru-COUPY** inhibited cell viability to some degree upon light irradiation except for 770 nm light, where photocytotoxicity showed no difference with respect to dark cytotoxicity (Fig. 4b). For light treatments within the red spectral zone, *i.e.*, 620 to 670 nm, **COUPY**, **Ru** and **PpIX** yielded submicromolar activity, whereas light IC_{50} values for **Ru-COUPY** ranged from 1 to 4 μM (Fig. 4b and Table S4†). Interestingly, when using NIR light at 740 nm, **COUPY** and **Ru** antiproliferative activity decreased by 10-fold compared to red-light treatments, **PpIX** did not show any NIR-photocytotoxicity up to 300 μM, but **Ru-COUPY** conjugate, in contrast, provided cell killing upon 740 nm irradiation (light IC_{50} = 7 μM) in the same micromolar range as with other red-light treatments (Fig. 4b and S11†).

Regarding to PI values, we found that the photoactivity matched with the wavelength range where the compounds absorb light (Fig. 4c). Overall, the PI potency decreased upon increasing wavelength treatments. For example, **Ru** compound retained decent anticancer photoactivity upon 620 nm (PI = 39), but the PI potency decreased with longer wavelengths (13 with 645 nm light, 6 with 670 nm light and 5 with 740 nm light treatment). PI values for **COUPY** ranged between 45 and 73 with red light but also diminished to 6 when applying 740 nm light. In comparison with its precursors, **Ru-COUPY** conjugate exerted higher photoactivity with all light regimens, providing PI values larger than **Ru** or **COUPY**. For instance, 645 nm light treatment yielded PI values for **Ru-COUPY** that were at least 4-fold higher than **COUPY** treatment with this wavelength and 20-fold higher that of **Ru**. At longer wavelengths, PI potency of **Ru-COUPY** was slightly attenuated. Intriguingly, marked photoactivation was observed with 740 nm light (PI > 42) with **Ru-COUPY**. A similar trend was found for the clinical drug **PpIX**, which exhibited highly potent photoactivation with 645 nm light (PI > 7500) that was attenuated with 670 nm light treatment (PI > 500). However, **PpIX** was completely inactive upon 740 nm light irradiation.

2.4.4. NIR-photocytotoxicity in hypoxia. Benefiting from the good phototherapeutic profile of **Ru-COUPY** using NIR light, we proceeded to examine its efficiency under PDT-challenging hypoxia condition (2% O_2), as previously performed with other PSs based on Os complexes.[78] This severe anaerobic state

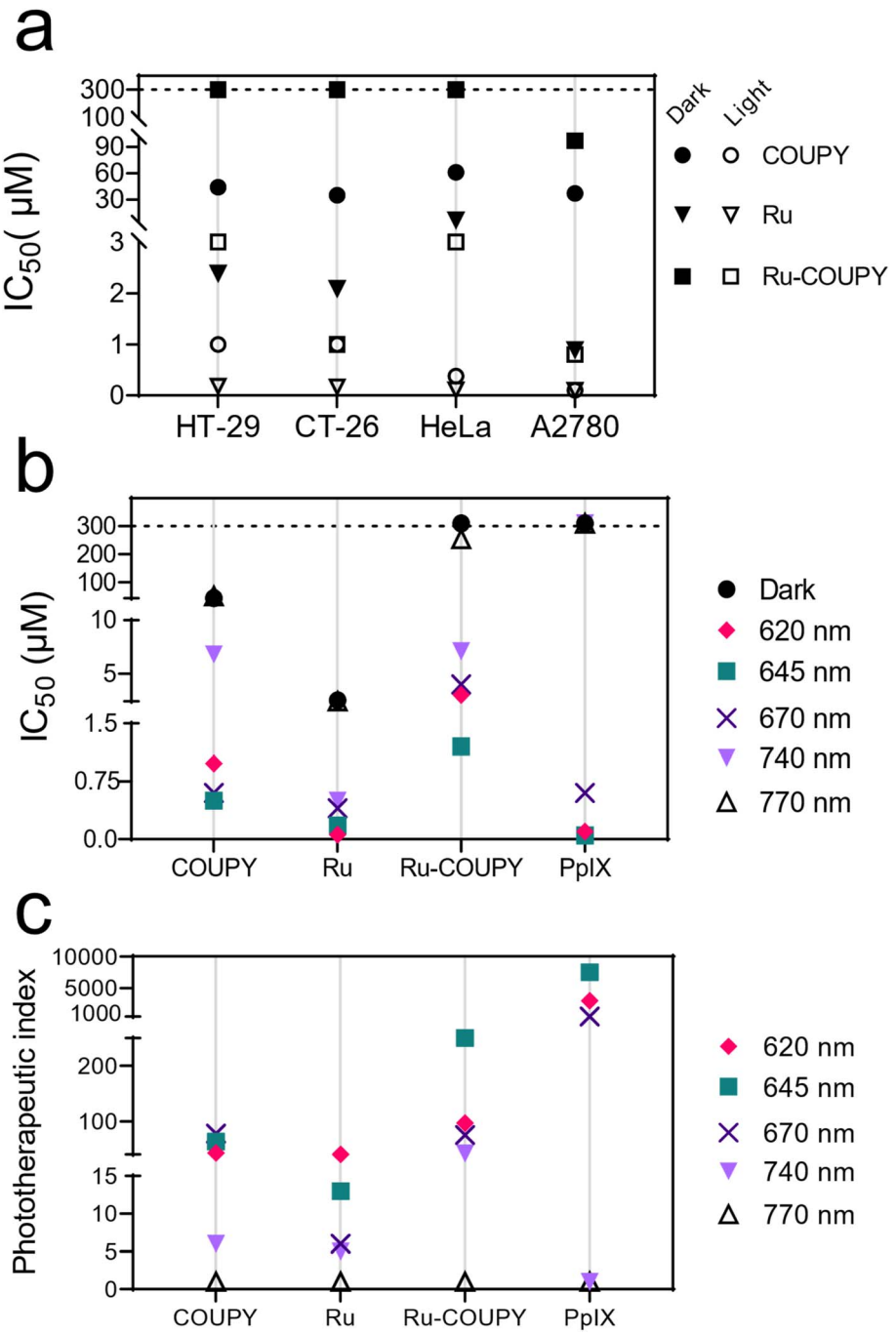

Fig. 4 Photocytotoxicity and chromatic screening in cancer cells. (a) Summary of *in vitro* photocytotoxicity for **COUPY**, **Ru** and **Ru-COUPY** compounds in cancer cell lines after red light irradiation (620 nm, 60 mW cm^{-2}, 1 h). IC_{50} values and their corresponding SD errors are tabulated in Table S3.† (b and c) Chromatic screening of the compounds from 620 nm to 770 nm in HT-29 cells represented as IC_{50} and phototherapeutic index values, defined as the ratio of dark to light IC_{50} values. These values and their corresponding SD errors are tabulated in Table S4.†

environment was achieved by using a hypoxia chamber glove box in which the temperature-controlled irradiation device platform was placed. The photocytotoxicity in hypoxia was assessed against HT-29 cells both in the dark and under NIR light irradiation (740 nm).

In general, the low oxygen tension of the hypoxia condition resulted in higher IC_{50} values and smaller PI values for the PSs herein studied (Fig. 5a and b and Table S5†). As depicted in Fig. 5a, oxygen tension had little to no impact on dark cytotoxicity. Upon 740 nm irradiation, 2% O_2 overwhelmed PDT activity of **Ru** and **COUPY** precursors. However, as shown in Fig. 5a and b and Fig. S12,† **Ru-COUPY** treatment still retained reasonable anticancer photoactivity under hypoxia (light IC_{50} value of 13 μM and PI > 23), whereas **PpIX** was utterly inactive (light IC_{50} > 300 μM). To illustrate the oxygen-dependence of the investigated PSs, a hypoxia index (HI), defined as the ratio from

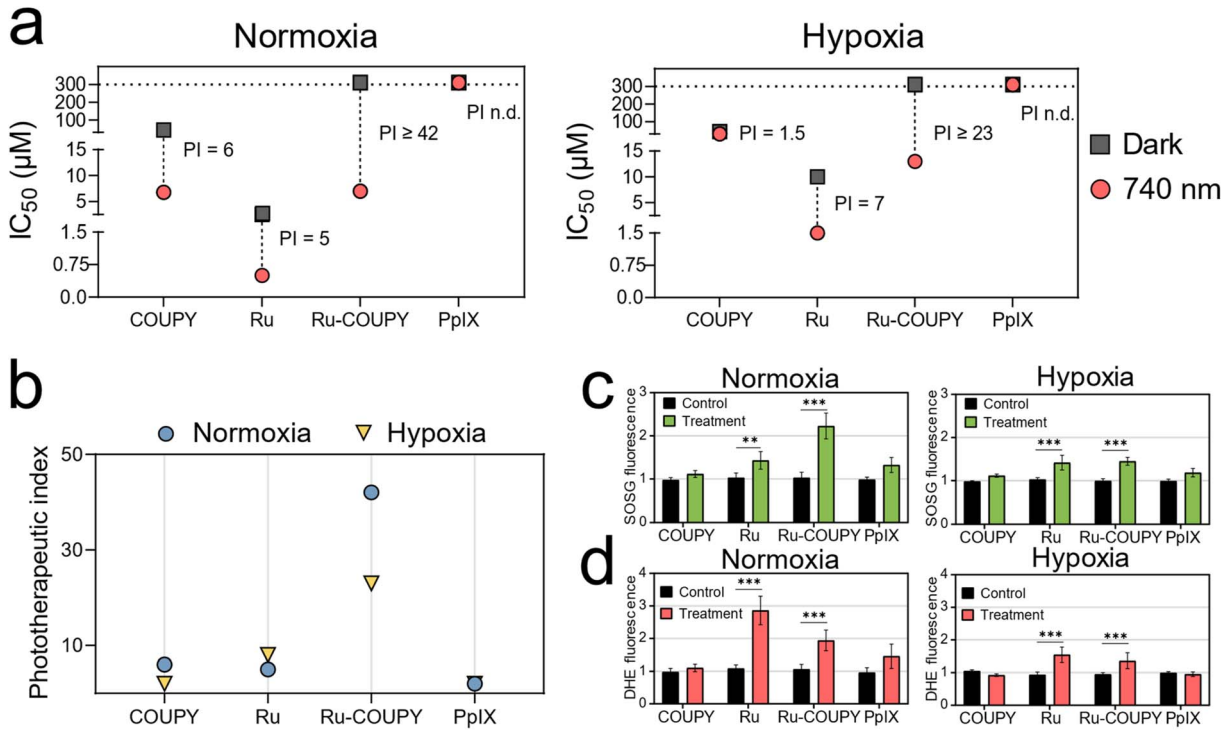

Fig. 5 NIR-photocytotoxicity and photogeneration of ROS under hypoxia. (a) *In vitro* photocytotoxicity in HT-29 for **COUPY**, **Ru**, **Ru-COUPY** and **PpIX** after NIR light irradiation (740 nm, 100 mW cm^{-2}, 1 h) under normoxia (21% O_2) and hypoxia (2% O_2). Half-maximal inhibitory concentration (IC_{50}) and phototherapeutic index (PI) values and their corresponding SD errors are tabulated in the ESI in Table S6.† (b) Summary of NIR phototherapeutic indexes of the compounds in HT-29 cells. (c and d) Singlet oxygen and superoxide levels in HT-29 after 740 nm light irradiation in normoxia and hypoxia as measured by Singlet Oxygen Sensor Green (SOSG, 5 μM for 0.5 h) and dihydroethidium (DHE, 10 μM for 0.5 h) probes, respectively. Control: irradiated, non-treated cells; treatment: irradiated, treated cells (10 μM). Data expressed as mean ± SD from three independent experiments. Statistical significance determined *via* one-way ANOVA test (*$p < 0.05$; **$p < 0.01$ and ***$p < 0.001$).

light IC_{50} in normoxia to hypoxia, was calculated (Table S6†). This index provides an idea of the hypoxia potency of a given PS under hypoxia compared to normoxia. For instance, the HI for **COUPY** was 5, meaning a 5-fold loss in photocytotoxicity when changing from normal-to low-oxygen conditions. **Ru** precursor had better hypoxia performance, with HI of 3, but still showed dark cytotoxicity (dark IC_{50} = 11 μM). **Ru-COUPY**, however, yielded a HI even closer to 1 (HI = 1.8) while showed no toxicity in the dark up to 300 μM.

2.4.5. NIR light-triggered ROS. At this point, the cellular mechanism of action of the PDT agents herein investigated was evaluated. Central to type II PDT pathway is the generation of singlet oxygen ($^1O_2$) from molecular oxygen (Fig. 1a).[79] Singlet oxygen is one of the most toxic ROS and is considered as a main photosensitization mechanism.[79] We detected intracellular $^1O_2$ photogeneration by using singlet oxygen sensor green (SOSG), whereas dihydroethidium (DHE) was utilized to probe superoxide anion ($O_2^{\bullet-}$) levels as a measure of type I-PDT contributions to photocytotoxicity. As shown in Fig. 5c, only Ru-containing compounds, *i.e.*, **Ru** and **Ru-COUPY**, produced $^1O_2$ upon NIR light irradiation, whereas **COUPY** did not at equitoxic concentrations. This photogeneration was dose-dependent and, due to its inherent dependence on molecular oxygen, also diminished in hypoxia (Fig. 5c and S13†). As expected, **PpIX** did not photogenerated $^1O_2$ neither in normoxia nor in hypoxia since no photoactivation was observed with 740 nm light (Fig. S12†). On the other hand, experiments with DHE probe showed a similar trend, with only **Ru** and **Ru-COUPY** raising superoxide levels anions at 10 μM after NIR light irradiation (Fig. 5c). A dose-dependent relationship was also observed under both normoxia and hypoxia, with smaller increases in the latter situation (Fig. S14†). Notably, remarkable DHE fluorescence for $O_2^{\bullet-}$ was detected using **Ru** at 1 μM and 5 μM concentrations even under hypoxia. In normoxia, irradiation of **Ru-COUPY** at 5 μM significantly boosted the levels of $O_2^{\bullet-}$ as compared to control cells, but such increment was not found under hypoxia. In contrast, negligible changes in DHE fluorescence were found upon PDT treatment with **COUPY** or **PpIX** in normoxia or hypoxia.

3. Discussion

Recent endeavours in PDT *via* light-induced electron transfer (type I mechanism) or energy transfer (type II mechanism) have led to the improvement of organic- and metal-based PSs for anticancer phototherapy. However, despite these achievements, the development of new PSs faces formidable challenges such as dark cytotoxicity, light penetration issues and poor photoactivity under hypoxia, which limit the effectiveness of PDT in the clinics to treat a wide spectrum of deep-seated tumors. To

overcome these limitations, the present study defines a strategy for achieving efficient anticancer PDT with a novel NIR-activatable PS based on the conjugation of a cyclometalated Ru(II) polypyridyl complex exhibiting prominent activity under hypoxia[75] to a NIR-absorbing COUPY derivative. This allowed us to push the absorption of the resulting PS beyond visible wavelengths typically used with conventional porphyrin- and chlorin-based PSs.

The activation of PSs at longer wavelengths is highly desirable for oncological PDT applications as it can afford relatively increased tissue penetration compared to light of shorter wavelengths.[24] However, although NIR light would only increase tissue penetration in some millimetres compared to, for example, far-red and deep-red light (effective optical penetration depth of 5–10 mm compared to 3–5 mm, respectively),[21–23] this increment might result crucial for the clinical success of PDT for several reasons. First, the use of longer wavelengths allows treatment for thicker tumors that some clinically-approved PSs cannot tackle. For example, the second-generation chlorin PS Talaporfin, which exhibits a red-shifted absorption band than first-generation porphyrin-based PS Photofrin, exerted a stronger antitumor effect against bronchogenic carcinomas with >1 cm in diameter when irradiated at longer wavelengths of light (664 nm for Talaporfin compared to 630 nm for Photofrin).[80] Second, irradiation at deep-red and NIR wavelengths avoid the absorption band of haemoglobin and may therefore increase the photodynamic efficacy.[24] When the penetration of light was compared in erythrocyte phantoms, which simulate *in vivo* conditions where highly absorbing haemoglobin molecules are present, it was found that 650 nm treatment beams penetrated deeper into such tissue models than the 630 nm light.[81] Although this depth gain was slight, the increased penetration along with the higher absorption coefficient of Temoporfin would explain the superior photodynamic efficacy of Temoporfin (λ_{max} = 650 nm) over Photofrin (λ_{max} = 630 nm) observed in animal and clinical studies.[81] Third, it should be noted that the effective optical penetration depth is not equivalent to the effective treatment depth of PDT, such as the extent of necrosis depth.[82–84] The latter could be related to several penetration depths, depending on the total light applied, PS concentration and optical properties of the tissue.[82] In this regard, the use of light of longer wavelengths would result in greater effective treatment depths even if the optical penetration is limited to a few millimetres. Finally, wavelengths in the NIR window might guarantee the interstitial irradiation of difficult-to-reach anatomical locations such as the lungs, for example.[25] In such cases, peripheral lung neoplasms or small lung metastasis situated further from the bronchus might become more accessible to endoscopic fibres or catheters if longer wavelengths are used since light would be transmitted further throughout the air.[34,85] Taking into account all these considerations, we decided to explore the photoactivity retention of the Ru(II)-coumarin dyad at light wavelengths beyond the red region of the spectrum such as those in the NIR window, and compared it with the clinical drug **PpIX**.

Our strategy to access the NIR window was to tune the coumarin scaffold in order to modulate the photophysical properties of the COUPY fluorophore and, consequently, of the new Ru(II)-COUPY PS (Fig. 1 and 2). Worthy of note, these modifications could be achieved through minimal changes on the chemical structure without altering the overall molecular size, which add emphasis on how the COUPY scaffold can be easily modified for this purpose. **Ru-COUPY** conjugate offered several advantages for PDT: (1) high aqueous solubility and stability in biological media (Fig. S4†), which are desirable properties for potential parenteral route administration, (2) photostability, an important requirement for PSs (Fig. S5†), (3) biocompatibility since excellent cell internalization was observed in cancer cells (Fig. 3a), and (4) operability in the phototherapeutic window (Table S4†). Indeed, cellular uptake studies showed that **Ru-COUPY** rapidly internalized in cancer cells without the need of energy-dependent transport (Fig. 3b). While confocal microscopy revealed that **Ru-COUPY** was mostly found as bright punctate vesicles around the cytoplasm (Fig. 3a), ICP-MS analysis indicated that 65% of the ruthenium content was trapped in the cytoskeleton fraction of the cells (Fig. S6†), suggesting that **Ru-COUPY** might preferentially target cytoskeletal proteins, which are distributed across the cytoplasm and involved in cell shape, compartmentalization and intracellular cargo trafficking.[86] In agreement with the assessment by confocal microscopy, ICP-MS also confirmed that **Ru-COUPY** accumulated in cell membranes to a lesser extent. This pattern of distribution was different from that of its unconjugated **COUPY** counterpart, which accumulated in mitochondria, but was somewhat similar to that of **Ru** (Fig. S6†). However, the percentage of ruthenium found in membrane fractions from **Ru** treatment was twice the amount found when cells were treated with **Ru-COUPY** (Fig. S6†). This membrane-association ability was coherent with the calculated log*P* values (Table S1†), as **Ru** was more lipophilic than the conjugate. Overall, this difference in intracellular compound distribution might explain the substantial reduction in **Ru-COUPY** dark cytotoxicity compared to **Ru** (Fig. 3c and S7†).

The prospect of developing **Ru-COUPY** was very appealing since conjugation not only reduced undesired dark toxicity but also increased phototherapeutic potency compared to **COUPY** and **Ru** complexes. With PI values greater than 1–3 × 10^2, **Ru-COUPY** exhibited better PDT activities than **Ru** or **COUPY** in almost all tested cell lines upon 620 nm light (Fig. 4a), which overlaps the maximum absorption of the conjugate, as well as of the longest absorption band of **PpIX**, the metabolite of the FDA approved 5-aminolevulinic acid drug (5-ALA).[38] This prompted us to test longer wavelengths in the deep-red, far-red and NIR regions, which possess deeper optical penetration into biological tissues and less attenuation during tissue propagation,[87] finding that **Ru-COUPY** could be activated with NIR light ($PI_{740\ nm}$ > 42). Notably, at NIR wavelengths **PpIX** showed no photocytotoxicity (Fig. 4b and c). The discovery of this NIR-activatable Ru(II)-coumarin conjugate means that anticancer photoactivation of Ru(II)-based PSs using wavelengths beyond the visible range can be easily achieved by the sole attachment of small-molecule, easily-modifiable **COUPY** coumarins; without the need of using more complex approaches based on two-photon excitation,[48] quantum dots[88] or upconversion nanoparticles.[89]

We then directed our attention on evaluating the hypoxia performance of the **Ru-COUPY** PS. Since hypoxia conditions slightly impaired the NIR PDT activity of **Ru-COUPY**, we hypothesized that type II oxygen-dependent pathway might be involved. Determination of $^1O_2$ levels in cancer cells confirmed this hypothesis, although **Ru-COUPY** still exhibited micromolar photocytotoxicity under hypoxia with an appealing PI > 23 and HI of ~2 (Fig. 5b and c and Table S5†). This validated that the photoactivity of **Ru-COUPY** was not entirely dependent on high concentrations of oxygen. Since spectroscopic studies using DHR123 pointed out to $O_2^{\bullet-}$ photogeneration, we further tested this in cells using the DHE probe. The results confirmed that PDT treatments with **Ru**-containing PSs (**Ru** and **Ru-COUPY**) raised intracellular $O_2^{\bullet-}$ radicals upon NIR irradiation, indicating that type I superoxide-generating photodynamic reactions might be taking place simultaneously (Fig. 5d). Although the levels of ROS produced in cancer cells were lower under hypoxia (Fig. S12 and S13†), the ability of this metal-coumarin dyad to simultaneously activate type I and type II photochemical pathways with NIR light could serve to alleviate the hypoxia limitation of conventional PDT. Furthermore, our cell-based studies suggested that ROS-generating PDT reactions would prompt to morphological aberrations and induction of apoptosis (Fig. S8–S10†). Altogether, **Ru-COUPY** conjugate with its NIR-photoactive properties and the photophysical and photobiological features herein studied is promising for further evaluation as a novel PDT agent.

4. Conclusions

In summary, a novel metal-based photosensitizer with potent anticancer photodynamic action was developed and successfully addressed some of the main issues of conventional PDT agents such as dark cytotoxicity and lack of operability under hypoxia with non-toxic and highly penetrating NIR light. The novel PS based on a Ru-coumarin conjugate exhibits water-solubility, dark stability in biological relevant media and high photostability along with advantageous luminescent properties that facilitate both bioimaging and phototherapy. Comprehensive photochemical characterizations were performed to assess the ability of the compound to simultaneously photogenerate type I superoxide anions and type II singlet oxygen, which were further confirmed by *in vitro* cellular studies in HT-29 colon cancer cells. These findings proved that **Ru-COUPY** could efficiently convert molecular oxygen into cytotoxic ROS triggered by low doses of NIR light irradiation (0.1 W cm^{-2}) even under severe anaerobic states (2% O_2), achieving high PI values and null dark toxicity toward cancer cells. Overall, this strategy could pave the way to the development of novel NIR- and hypoxia-active Ru(II)-based theragnostic PSs fuelled by the conjugation of tunable, low molecular-weight COUPY fluorophores.

5. Materials and methods

5.1 Synthesis and characterization of the compounds

Unless otherwise stated, common chemicals and solvents (HPLC grade or reagent grade quality) were purchased from commercial sources and used without further purification. A hot plate magnetic stirrer, together with an aluminum reaction block of the appropriate size, was used as the heating source in all reactions requiring heat. Aluminum plates coated with a 0.2 mm-thick layer of silica gel 60 F_{254} were used for thin-layer chromatography (TLC) analysis, whereas flash column chromatography purification was carried out using silica gel 60 (230–400 mesh). Proton (^{1}H) and proton-decoupled carbon (^{13}C{^{1}H}) NMR spectra were recorded at 25 °C in a 400 MHz spectrometer using the deuterated solvent as an internal deuterium lock. The residual protic signal of chloroform, MeOH or DMSO was used as a reference in ^{1}H and ^{13}C{^{1}H} NMR spectra recorded in $CDCl_3$, CD_3OD or DMSO-d_6, respectively. Chemical shifts are reported in parts per million (ppm) in the δ scale, coupling constants in Hz, and multiplicity as follows: s (singlet), d (doublet), t (triplet), q (quartet), qt (quintet), m (multiplet). Low-resolution electrospray ionization mass spectra (ESI-MS) were recorded on an instrument equipped with single quadrupole detector coupled to an HPLC and high-resolution (HR) ESI-MS on an LC/MS-TOF instrument. The purity of final compounds was determined by reversed-phase high performance liquid chromatography (HPLC) analyses on a Jupiter Proteo C12 column (250 × 4.6 mm, 90 Å, 4 μm, flow rate: 1 mL min^{-1}) (system A) or on a ACQUITY UPLC SCH™ C18 column (3.0 × 50 mm, 1.7 μm, flow rate: 1 mL min^{-1}) (system B) using linear gradients of 0.1% formic acid in Milli-Q H_2O (A) and 0.1% formic acid in ACN (B). The HPLC column was maintained at 25 °C. All final compounds were >95% pure by this method.

Description of the synthesis of the compounds herein investigated can be found in the ESI.†

5.2 Cell culture

HeLa and CT-26 cells were cultured in Dulbecco's modified Eagle medium (DMEM) supplemented with 10% fetal bovine serum (FBS) and 2 mM L-glutamine. A2780 cells were grown in RPMI-1640 cell medium with 10% FBS and 2 mM L-glutamine. HT-29 cells were maintained in McCoys medium with 10% FBS and 2 mM L-glutamine. All cell lines were supplemented with 100 U mL^{-1} penicillin–streptomycin mixture (Gibco) and maintained in a humidified atmosphere at 37 °C and 5% of CO_2. Subculture routine was performed two or three times a week with appropriate densities and cells were confirmed to be mycoplasma-free using a standard Hoechst DNA staining method.

5.3 Cellular accumulation by ICP-MS

Briefly, HT-29 cells were seeded onto 12-well plate (4 × 10^5 cells per well). Treatments with tested compounds were applied for 1 h at 10 μM either at 37 °C or at 4 °C. Cisplatin was included for comparison. Cells were then trypsinized, and pellets were counted. Samples were then digested with 30% HNO_3 suprapur acid (Sigma Aldrich) and subjected to Inductively Coupled Plasma Mass Spectrometry analysis in Agilent 7900 ICP-MS. ^{99}Ru, ^{101}Ru, ^{194}Pt and ^{195}Pt isotopes were measured. Three independent experiments were performed with $n = 2$ replicates.

5.4 Cellular uptake and confocal fluorescence imaging

For cellular uptake experiments and posterior observation under the microscope, cells were seeded on glass bottom dishes (P35G-1.5-14-C, Mattek). 24 h after cell seeding, cells were incubated at 37 °C for 30 min with **COUPY** (1 μM) and **Ru-COUPY** (10 μM) in supplemented DMEM. Then, cells were washed three times with DPBS (Dulbecco's phosphate-buffered saline) to remove the excess of the compounds and kept in DMEM with Hepes (10 mM) and without phenol red for fluorescence imaging. All microscopy observations were performed using a Zeiss LSM 880 confocal microscope equipped with a heating insert P S (Pecon) and using a 63×1.4 oil immersion objective. The compounds were excited using the 633 nm laser and detected from 650 to 750 nm. Image analysis was performed using Fiji.[90] Unless otherwise stated images are colorized using Fire lookup table.

5.5 Photocytotoxic activity determination

HT-29, CT-26, HeLa and A2780 cells were maintained at logarithmic growth-phase and transferred into 96-well plates at a density of 5000 cells per well in complete medium for 24 h at 37 °C, 5% CO_2 in a humidified incubator. For hypoxia experiments, a Hypoxia condition was set up using nitrogen (N_2) to displace O_2 down to a minimum of 2% in a Forma™ Steri-Cycle™ i160 incubator (ThermoFisher Scientific) and cells were cultured under hypoxia 2 weeks prior to experiments. Serial dilutions of the compounds were prepared in DMSO and added to cells at final concentrations in the range of 0 to 300 μM in a final volume of 100 μL per well (1% DMSO v/v). Light treatment schedule was performed as follows: 1 h incubation with the compounds in the dark, removal of compounds and addition of fresh media, followed by 1 h incubation under irradiation conditions using LED well plate irradiator (Atlas Photonics Lumos Bio). Light treatments were applied for 1 h with 620 nm (60 mW cm^{-2}), 645 nm (80 mW cm^{-2}), 670 nm (120 mW cm^{-2}), 740 nm (100 mW cm^{-2}) or 770 nm (110 mW cm^{-2}) well-by-well LED lamps. Spectral half-width for LED lamps: 620 nm (32 nm, 1.88 mW cm^{-2}), 645 nm (32 nm, 2.50 mW cm^{-2}), 670 nm (32 nm, 3.75 mW cm^{-2}), 740 nm (32 nm, 3.50 mW cm^{-2}) and 770 nm (32 nm, 6.75 mV cm^{-2}). In the case of hypoxia experiments, the hypoxia glove chamber (Plas Labs), in which the temperature-controlled light device was placed, was set up to 2%O_2 (Fig. S12†). All the cell culture plates subjected to light irradiation included untreated controls to verify that cell viability was not affected by light. Next, 24 h cell recovery period was allowed after irradiation; the temperature throughout the experiment remaining at 37 °C. Dark control samples were directly incubated for 1 h in the dark in the humidified CO_2 incubator either in normoxia or hypoxia. Alternatively, cytotoxicity from 24 h dark incubation without recovery period was also assayed in all cell lines. Medium was then aspirated by suction, and cells were loaded with 50 μL of resazurin solution (2 mg mL^{-1}) for additional 4 h. The fluorescence was measured at 590 nm using a microplate reader (Cytation™ 5; BioTek Instruments) and the IC_{50} values were calculated based on the inhibitory rate curves using the following equation:

$$I = \frac{I_{max}}{1 + \left(\frac{IC_{50}}{C}\right)^{n}}$$

where I represent the percentage inhibition of viability, I_{max} is the maximal inhibitory effect, IC_{50} is the concentration that inhibits 50% of maximal growth, C is the concentration of the treatment and n is the slope of the semi-logarithmic dose–response sigmoidal curves. The non-linear fitting was performed using SigmaPlot 14.0 software. All experiments were performed in three independent studies with $n = 3$ replicates per concentration level.

5.6 ROS photogeneration in cancer cells

Singlet oxygen levels were determined using the SOSG probe (Invitrogen). HT-29 cells were seeded onto 96-well plates at 2×10^4 cells per well for 24 h in a humidified CO_2 incubator either in normoxia (21% O_2) or hypoxia (2% O_2). Tested compounds were then administered in cell media for 1 h. Treatments were then removed, and cells were stained with 5 μM of SOSG for 0.5 h. After staining, cells were washed with PBS and irradiated for 1 h with 740 nm light using the LED well plate irradiator (Atlas Photonics Lumos Bio) at a final light intensity of 100 mW cm^{-2}. Fluorescence readings were performed in Cell Imaging Multimode Reader Cytation™ 5 (BioTek Instruments) using $\lambda_{exc/em}$ = 488/530 nm. Alternatively, superoxide levels were determined using DHE (ThermoFisher) following the same protocol but staining with this probe (10 μM for 0.5 h); readings being registered at $\lambda_{exc/em}$ = 518/606 nm. For both series of experiments, non-irradiated plates were used for dark conditions whereas treated, unstained cells were used to subtract basal fluorescence of compounds and correct fluorescence readings. Unstained cells served as blank. Irradiated, non-treated cells were used as control groups. Three independent experiments were performed with $n = 4$ replicates.

Author contributions

E. O.-F., V. M., M.-D. S., J. R. and G. G. conceived the research. E. O.-F., A. H. G. and F. B. synthesized the Ru complexes. A. R. and M. L.-C. synthesized and characterized the COUPY fluorophores and the Ru(II)-COUPYconjugate. A. R. and M. L.-C. investigated the photophysical and photochemical properties of the compounds. A. R., M. L.-C. and M. B. performed confocal microscopy studies. E. I.-G. performed superoxide determination experiments and log P determination. M. J.-R. and S. N. studied singlet oxygen generation and performed flash photolysis studies. E. O.-F. performed all photobiological experiments (cyto- and phototoxicity, ROS determination, cell death studies and cellular accumulation by ICP-MS). E. O.-F. wrote the manuscript, which was contributed by all authors. All authors have approved the final version of the manuscript.

Conflicts of interest

There are no conflicts to declare.

Acknowledgements

This work was supported by funds from the Spanish Ministerio de Ciencia e Innovación-Agencia Estatal de Investigación (MCI/AEI/10.13039/501100011033) and FEDER funds (Projects PID2020-117508RB-I00, PID2021-122850NB-I00 and PID2020-115801RB-C22). The stay of E. O.-F. in G. G. laboratory was funded by a scholarship from EIDUM-CMN of University of Murcia. This work was financially supported by an ERC Consolidator Grant Photo-MedMet to G. G. (GA 681679) and has received support under the program ''Investissements d'Avenir'' launched by the French Government and implemented by the ANR with the reference ANR-10-IDEX-0001-02 PSL (G. G.). E. O.-F thanks AECC (Project PRDMU19003ORTE). A. R. and M. L.-C. were recipient fellows of the University of Barcelona (APIF) and of the Generalitat de Catalunya (FI-SDUR), respectively. E. I.-G. acknowledges support from a Margarita Salas University of Barcelona postdoctoral grant funded by the Spanish Ministerio de Universidades with European Union funds – NextGenerationEU. The authors acknowledge helpful assistance from Dr Francisco Cárdenas (NMR) and Dr Irene Fernández and Laura Ortiz (MS) from CCiTUB.

References

1 D. E. J. G. J. Dolmans, D. Fukumura and R. K. Jain, *Nat. Rev. Cancer*, 2003, **3**, 380–387.
2 R. Baskaran, J. Lee and S.-G. Yang, *Biom. Res.*, 2018, **22**, 25.
3 K.-X. Teng, W.-K. Chen, L.-Y. Niu, W.-H. Fang, G. Cui and Q.-Z. Yang, *Angew. Chem., Int. Ed.*, 2021, **60**, 19912–19920.
4 Y. Wan, L.-H. Fu, C. Li, J. Lin and P. Huang, *Adv. Mat.*, 2021, **33**, 2103978.
5 F. Wei, T. W. Rees, X. Liao, L. Ji and H. Chao, *Coord. Chem. Rev.*, 2021, **432**, 213714.
6 J. A. Roque, P. C. Barrett, H. D. Cole, L. M. Lifshits, G. Shi, S. Monro, D. von Dohlen, S. Kim, N. Russo, G. Deep, C. G. Cameron, M. E. Alberto and S. A. McFarland, *Chem. Sci.*, 2020, **11**, 9784–9806.
7 J. A. I. Roque, P. C. Barrett, H. D. Cole, L. M. Lifshits, E. Bradner, G. Shi, D. von Dohlen, S. Kim, N. Russo, G. Deep, C. G. Cameron, M. E. Alberto and S. A. McFarland, *Inorg. Chem.*, 2020, **59**, 16341–16360.
8 N. Lu, Z. Deng, J. Gao, C. Liang, H. Xia and P. Zhang, *Nat. Commun.*, 2022, **13**, 2245.
9 M. Li, J. Xia, R. Tian, J. Wang, J. Fan, J. Du, S. Long, X. Song, J. W. Foley and X. Peng, *J. Am. Chem. Soc.*, 2018, **140**, 14851–14859.
10 S. Kuang, L. Sun, X. Zhang, X. Liao, T. W. Rees, L. Zeng, Y. Chen, X. Zhang, L. Ji and H. Chao, *Angew. Chem., Int. Ed.*, 2020, **59**, 20697–20703.
11 S. Kuang, F. Wei, J. Karges, L. Ke, K. Xiong, X. Liao, G. Gasser, L. Ji and H. Chao, *J. Am. Chem. Soc.*, 2022, **144**, 4091–4101.
12 M. Li, T. Xiong, J. Du, R. Tian, M. Xiao, L. Guo, S. Long, J. Fan, W. Sun, K. Shao, X. Song, J. W. Foley and X. Peng, *J. Am. Chem. Soc.*, 2019, **141**, 2695–2702.
13 S. Bonnet, *Dalton Trans.*, 2018, **47**, 10330–10343.
14 B. S. Howerton, D. K. Heidary and E. C. Glazer, *J. Am. Chem. Soc.*, 2012, **134**, 8324–8327.
15 Z. Wang, N. Wang, S.-C. Cheng, K. Xu, Z. Deng, S. Chen, Z. Xu, K. Xie, M.-K. Tse, P. Shi, H. Hirao, C.-C. Ko and G. Zhu, *Chem*, 2019, **5**, 3151–3165.
16 Z. Wang, Z. Deng and G. Zhu, *Dalton Trans.*, 2019, **48**, 2536–2544.
17 J. D. Knoll, B. A. Albani and C. Turro, *Acc. Chem. Res.*, 2015, **48**, 2280–2287.
18 J. Roque III, D. Havrylyuk, P. C. Barrett, T. Sainuddin, J. McCain, K. Colón, W. T. Sparks, E. Bradner, S. Monro, D. Heidary, C. G. Cameron, E. C. Glazer and S. A. McFarland, *Photochem. Photobiol.*, 2020, **96**, 327–339.
19 H. D. Cole, J. A. Roque, L. M. Lifshits, R. Hodges, P. C. Barrett, D. Havrylyuk, D. Heidary, E. Ramasamy, C. G. Cameron, E. C. Glazer and S. A. McFarland, *Photochem. Photobiol.*, 2022, **98**, 73–84.
20 C. Zhang, R. Guan, X. Liao, C. Ouyang, T. W. Rees, J. Liu, Y. Chen, L. Ji and H. Chao, *Chem. Commun.*, 2019, **55**, 12547–12550.
21 M. M. Kim and A. Darafsheh, *Photochem. Photobiol.*, 2020, **96**, 280–294.
22 M. V. Padalkar and N. Pleshko, *Analyst*, 2015, **140**, 2093–2100.
23 V. V. Barun, A. P. Ivanov, A. V. Volotovskaya and V. S. Ulashchik, *J. Appl. Spectrosc.*, 2007, **74**, 430–439.
24 K. Plaetzer, B. Krammer, J. Berlanda, F. Berr and T. Kiesslich, *Lasers Med. Sci.*, 2009, **24**, 259–268.
25 X. Li, J. F. Lovell, J. Yoon and X. Chen, *Nat. Rev. Clin. Oncol.*, 2020, **17**, 657–674.
26 A. Yuan, J. Wu, X. Tang, L. Zhao, F. Xu and Y. Hu, *J. Pharm. Sci.*, 2013, **102**, 6–28.
27 S. W. Young, K. W. Woodburn, M. Wright, T. D. Mody, Q. Fan, J. L. Sessler, W. C. Dow and R. A. Miller, *Photochem. Photobiol.*, 1996, **63**, 892–897.
28 M. Mitsunaga, M. Ogawa, N. Kosaka, L. T. Rosenblum, P. L. Choyke and H. Kobayashi, *Nat. Med.*, 2011, **17**, 1685–1691.
29 H. Kostron and T. Hasan, *Photodynamic Medicine: From Bench to Clinic*, Royal Society of Chemistry, Cambridge (UK), 2016.
30 L. L. Santos, J. Oliveira, E. Monteiro, J. Santos and C. Sarmento, *Case Rep. Oncol.*, 2018, **11**, 769–776.
31 A.-R. Azzouzi, S. Vincendeau, E. Barret, A. Cicco, F. Kleinclauss, H. G. van der Poel, C. G. Stief, J. Rassweiler, G. Salomon, E. Solsona, A. Alcaraz, T. T. Tammela, D. J. Rosario, F. Gomez-Veiga, G. Ahlgren, F. Benzaghou, B. Gaillac, B. Amzal, F. M. J. Debruyne, G. Fromont, C. Gratzke and M. Emberton, *Lancet Oncol.*, 2017, **18**, 181–191.
32 H. O. Alsaab, M. S. Alghamdi, A. S. Alotaibi, R. Alzhrani, F. Alwuthaynani, Y. S. Althobaiti, A. H. Almalki, S. Sau and A. K. Iyer, *Cancers*, 2020, **12**, 2793.
33 A. Akopov and G. Papayan, *Photodiagn. Photodyn. Ther.*, 2021, **33**, 102203.
34 K. Sato, T. Nagaya, M. Mitsunaga, P. L. Choyke and H. Kobayashi, *Cancer Lett.*, 2015, **365**, 112–121.

35 S. Wang, E. Bromley, L. Xu, J. C. Chen and L. Keltner, *Expert Opin. Pharmacother.*, 2010, **11**, 133–140.
36 N. W. N. Simelane, C. A. Kruger and H. Abrahamse, *RSC Adv.*, 2020, **10**, 41560–41576.
37 G. Gunaydin, M. E. Gedik and S. Ayan, *Front. Chem.*, 2021, **9**, 686303.
38 R. R. Allison and C. H. Sibata, *Photodiagn. Photodyn. Ther.*, 2010, **7**, 61–75.
39 D. van Straten, V. Mashayekhi, H. S. de Bruijn, S. Oliveira and D. J. Robinson, *Cancers*, 2017, **9**, 19.
40 S. Chamberlain, H. D. Cole, J. Roque, D. Bellnier, S. A. McFarland and G. Shafirstein, *Pharmaceuticals*, 2020, **13**, 137.
41 S. Monro, K. L. Colón, H. Yin, J. Roque, P. Konda, S. Gujar, R. P. Thummel, L. Lilge, C. G. Cameron and S. A. McFarland, *Chem. Rev.*, 2019, **119**, 797–828.
42 J. Li and T. Chen, *Coord. Chem. Rev.*, 2020, **418**, 213355.
43 A. Zamora, G. Vigueras, V. Rodríguez, M. D. Santana and J. Ruiz, *Coord. Chem. Rev.*, 2018, **360**, 34–76.
44 S. A. McFarland, A. Mandel, R. Dumoulin-White and G. Gasser, *Curr. Opin. Chem. Biol.*, 2019, **56**, 23–27.
45 M. He, F. Chen, D. Shao, P. Weis, Z. Wei and W. Sun, *Biomaterials*, 2021, **275**, 120915.
46 C.-P. Tan, Y.-M. Zhong, L.-N. Ji and Z.-W. Mao, *Chem. Sci.*, 2021, **12**, 2357–2367.
47 M. Martínez-Alonso, A. Gandioso, C. Thibaudeau, X. Qin, P. Arnoux, N. Demeubayeva, V. Guérineau, C. Frochot, A. C. Jung, C. Gaiddon and G. Gasser, *ChemBioChem*, 2023, e202300203.
48 L. K. McKenzie, H. E. Bryant and J. A. Weinstein, *Coord. Chem. Rev.*, 2019, **379**, 2–29.
49 C. Imberti, P. Zhang, H. Huang and P. J. Sadler, *Angew. Chem., Int. Ed.*, 2020, **59**, 61–73.
50 Y. Wu, S. Li, Y. Chen, W. He and Z. Guo, *Chem. Sci.*, 2022, **13**, 5085–5106.
51 L. He, Y. Li, C.-P. Tan, R.-R. Ye, M.-H. Chen, J.-J. Cao, L.-N. Ji and Z.-W. Mao, *Chem. Sci.*, 2015, **6**, 5409–5418.
52 Y.-F. Zhong, H. Zhang, G. Mu, W.-T. Liu, Q. Cao, C.-P. Tan, L.-N. Ji and Z.-W. Mao, *Inorg. Chem. Front.*, 2019, **6**, 2817–2823.
53 J. Liu, C. Zhang, T. W. Rees, L. Ke, L. Ji and H. Chao, *Coord. Chem. Rev.*, 2018, **363**, 17–28.
54 H. Huang, S. Banerjee and P. J. Sadler, *ChemBioChem*, 2018, **19**, 1574–1589.
55 W. Fan, P. Huang and X. Chen, *Chem. Soc. Rev.*, 2016, **45**, 6488–6519.
56 X. Zhao, J. Liu, J. Fan, H. Chao and X. Peng, *Chem. Soc. Rev.*, 2021, **50**, 4185–4219.
57 P. Majumdar, X. Yuan, S. Li, B. L. Guennic, J. Ma, C. Zhang, D. Jacquemin and J. Zhao, *J. Mater. Chem. B*, 2014, **2**, 2838–2854.
58 E. Palao, R. Sola-Llano, A. Tabero, H. Manzano, A. R. Agarrabeitia, A. Villanueva, I. López-Arbeloa, V. Martínez-Martínez and M. J. Ortiz, *Chem. - Eur. J.*, 2017, **23**, 10139–10147.
59 L. Tabrizi and H. Chiniforoshan, *RSC Adv.*, 2017, **7**, 34160–34169.
60 L. Qiao, J. Liu, S. Kuang, X. Liao, J. Kou, L. Ji and H. Chao, *Dalton Trans.*, 2021, **50**, 14332–14341.
61 L. Zhang, Y. Geng, L. Li, X. Tong, S. Liu, X. Liu, Z. Su, Z. Xie, D. Zhu and M. R. Bryce, *Chem. Sci.*, 2021, **12**, 5918–5925.
62 Y. Wu, J. Wu and W.-Y. Wong, *Biomater. Sci.*, 2021, **9**, 4843–4853.
63 C. Liu, L. Zhou, F. Wei, L. Li, S. Zhao, P. Gong, L. Cai and K. M.-C. Wong, *ACS Appl. Mater. Interfaces*, 2019, **11**, 8797–8806.
64 V. Novohradsky, A. Rovira, C. Hally, A. Galindo, G. Vigueras, A. Gandioso, M. Svitelova, R. Bresolí-Obach, H. Kostrhunova, L. Markova, J. Kasparkova, S. Nonell, J. Ruiz, V. Brabec and V. Marchán, *Angew. Chem., Int. Ed.*, 2019, **58**, 6311–6315.
65 Z. Lv, H. Wei, Q. Li, X. Su, S. Liu, K. Y. Zhang, W. Lv, Q. Zhao, X. Li and W. Huang, *Chem. Sci.*, 2018, **9**, 502–512.
66 L. Qiao, J. Liu, Y. Han, F. Wei, X. Liao, C. Zhang, L. Xie, L. Ji and H. Chao, *Chem. Commun.*, 2021, **57**, 1790–1793.
67 M. J. Rose, M. M. Olmstead and P. K. Mascharak, *J. Am. Chem. Soc.*, 2007, **129**, 5342–5343.
68 O. Filevich, B. García-Acosta and R. Etchenique, *Photochem. Photobiol. Sci.*, 2012, **11**, 843–847.
69 N. P. Toupin, S. J. Steinke, M. K. Herroon, I. Podgorski, C. Turro and J. J. Kodanko, *Photochem. Photobiol.*, 2022, **98**, 378–388.
70 A. Rovira, M. Pujals, A. Gandioso, M. López-Corrales, M. Bosch and V. Marchán, *J. Org. Chem.*, 2020, **85**, 6086–6097.
71 A. Gandioso, R. Bresolí-Obach, A. Nin-Hill, M. Bosch, M. Palau, A. Galindo, S. Contreras, A. Rovira, C. Rovira, S. Nonell and V. Marchán, *J. Org. Chem.*, 2018, **83**, 1185–1195.
72 A. Rovira, E. Ortega-Forte, C. Hally, M. Jordà-Redondo, D. Abad-Montero, G. Vigueras, J. I. Martínez, M. Bosch, S. Nonell, J. Ruiz and V. Marchán, *J. Med. Chem.*, 2023, DOI: **10.1021/acs.jmedchem.3c00189**.
73 E. Ortega-Forte, A. Rovira, A. Gandioso, J. Bonelli, M. Bosch, J. Ruiz and V. Marchán, *J. Med. Chem.*, 2021, **64**, 17209–17220.
74 V. Novohradsky, L. Markova, H. Kostrhunova, J. Kasparkova, J. Ruiz, V. Marchán and V. Brabec, *Chem. - Eur. J.*, 2021, **27**, 8547–8556.
75 F. J. Ballester, E. Ortega, D. Bautista, M. D. Santana and J. Ruiz, *Chem. Commun.*, 2020, **56**, 10301–10304.
76 J. Karges, P. Goldner and G. Gasser, *Inorganics*, 2019, **7**, 4.
77 T. Mishchenko, I. Balalaeva, A. Gorokhova, M. Vedunova and D. V. Krysko, *Cell Death Dis.*, 2022, **13**, 1–16.
78 A. Mani, T. Feng, A. Gandioso, R. Vinck, A. Notaro, L. Gourdon, P. Burckel, B. Saubaméa, O. Blacque, K. Cariou, J.-E. Belgaied, H. Chao and G. Gasser, *Angew. Chem., Int. Ed.*, 2023, **62**, e202218347.
79 M. S. Baptista, J. Cadet, P. D. Mascio, A. A. Ghogare, A. Greer, M. R. Hamblin, C. Lorente, S. C. Nunez, M. S. Ribeiro, A. H. Thomas, M. Vignoni and T. M. Yoshimura, *Photochem. Photobiol.*, 2017, **93**, 912–919.
80 J. Usuda, S. Ichinose, T. Ishizumi, H. Hayashi, K. Ohtani, S. Maehara, S. Ono, H. Honda, N. Kajiwara, O. Uchida,

H. Tsutsui, T. Ohira, H. Kato and N. Ikeda, *Clin.Cancer Res.*, 2010, **16**, 2198–2204.
81 S. Mitra and T. H. Foster, *Photochem. Photobiol.*, 2005, **81**, 849–859.
82 B. W. Henderson and T. Dougherty, *Photodynamic Therapy: Basic Principles and Clinical Applications*, CRC Press, 1st edn, 1992.
83 K. Guidolin, L. Ding, H. Yan, M. Englesakis Hba, S. Chadi, F. Quereshy and G. Zheng, *Surg. Innov.*, 2022, **29**, 788–803.
84 D. Kessel and N. L. Oleinick, *Photochem. Photobiol.*, 2018, **94**, 213–218.
85 T. Okunaka, H. Kato, H. Tsutsui, T. Ishizumi, S. Ichinose and Y. Kuroiwa, *Lung Cancer*, 2004, **43**, 77–82.
86 D. A. Fletcher and R. D. Mullins, *Nature*, 2010, **463**, 485–492.
87 S. Stolik, J. A. Delgado, A. Pérez and L. Anasagasti, *J. Photochem. Photobiol., B*, 2000, **57**, 90–93.
88 S. S. Lucky, K. C. Soo and Y. Zhang, *Chem. Rev.*, 2015, **115**, 1990–2042.
89 C. Wang, L. Cheng and Z. Liu, *Theranostics*, 2013, **3**, 317–330.
90 J. Schindelin, I. Arganda-Carreras, E. Frise, V. Kaynig, M. Longair, T. Pietzsch, S. Preibisch, C. Rueden, S. Saalfeld, B. Schmid, J.-Y. Tinevez, D. J. White, V. Hartenstein, K. Eliceiri, P. Tomancak and A. Cardona, *Nat. Methods*, 2012, **9**, 676–682.